This is a post-peer-review, pre-copyedit version of an article published in Applied Clay Science. The final authenticated version is available online at:

https://doi.org/10.1016/j.clay.2021.106266

Encapsulation of butylimidazole in smectite and slow release for enhanced copper corrosion inhibition

Baudelaire Matangouo,[a] Gustave Kenne Dedzo,[a]* Liva Dzene,[b] Charles Péguy Nanseu-Njiki [a] and Emmanuel Ngameni [a]

[1]Laboratory of Analytical Chemistry, Faculty of Science, University of Yaoundé I, B.P. 812, Yaoundé, Cameroon

[2]Institut de Science des Matériaux de Mulhouse CNRS UMR 7361, Université de Haute-Alsace, Université de Strasbourg, 3b rue Alfred Werner, 68093 Mulhouse, Cedex, France

*E-mail: kennegusto@yahoo.fr

Abstract

Butylimidazole (Bim) a well-known copper corrosion inhibitor was encapsulated in its cationic form, in a smectite type clay mineral (Sabga clay mineral (Sg)) by cation exchange of sodium cations located in the interlayer space of the layered clay mineral. Physicochemical characterization (XRD, FT-IR and TGA) revealed that Bim was intercalated (0.48 mmol per gram of hybrid material) in its cationic form. The intercalation was followed by an increase of the layer to layer distance from 11.4 Å to 13.9 Å. The composite material (Sg-Bim) was then applied as copper corrosion inhibitor in concentrated sodium sulphate solution (0.1 M) and experiments monitored electrochemically. For a given concentration of Sg-Bim, the corrosion potential increased as a function of time. The corrosion inhibition percentages obtained both

by corrosion current densities (up to 80.7%) and charge transfer resistance (up to 87.0%) were found to increase with the release time. This confirmed that the clay mineral Sg effectively served as a nanocontainer for the encapsulation of Bim. Moreover, the release of Bim occurred gradually when the organoclay was immersed in concentrated saline solution. Investigations on the effect of temperature on the process confirmed that the action of released Bim against copper corrosion consisted in improving the stability of the Cu_2O protecting layer, according to a physisorption mechanism.

Keywords : copper corrosion, smectite intercalation, nanocontainer, butylimidazole, slow release.

1. Introduction

There are several strategies to protect metals against corrosion. One of the most popular methods developed these last years is the use of corrosion inhibitors (Gece, 2008). Corrosion inhibitors are substances capable even at low concentration, to slow down the rate of metals degradation by disrupting the electrochemical mechanisms of corrosion. This is generally achieved by limiting the direct access of the corrosive substance to the metal surface. Inorganic compounds such as chromates were found to be the most effective corrosion inhibitors. Unfortunately, they exhibit high environmental toxicity (Yuan et al., 2010; Winkler et al., 2016; Tchio et al., 2020). Several works demonstrate that some organic compounds can act as corrosion inhibitors (Verma et al., 2020; Damej et al., 2021). When chosen wisely, they are efficient and by far less polluting than inorganic inhibitors. Some of these organic corrosion inhibitors are synthetic compounds whose productions are not eco-friendly. To address this drawback, less polluting plant extracts were successfully applied as corrosion inhibitors (Bidi et al., 2021; Ngouné et al., 2019). However, their massive use is difficult to implement as significant environmental damages (massive use of fertilizers and pesticides amongst other) associated to the production of plants should be considered. The development of strategies to minimize the amount of organic inhibitors used for metals protection is an interesting alternative to reduce the environmental impact. One promising strategy is the encapsulation of corrosion inhibitors into microreactors. This approach allowed the control of the amount of inhibitor used, by releasing only the quantities necessary for optimal protection of the metal. In addition, it would be possible in very sophisticated systems to trigger the controlled release of the inhibitor according to the need of the system (Wang and Zhang, 2011; Aghzzaf et al., 2012).

While interesting, this approach is limited by the encapsulation devices available. The most common are organic nanovesicles (micelles, polymers, etc.), mesoporous silicas and layered double hydroxides (Truc et al., 2008; Aghzzaf et al., 2012). These reservoirs are synthetic

materials and require the use of expensive and polluting chemicals for their synthesis. Nature is full of stable and robust structures that have showed interesting results as nanocarriers. These are clay minerals such as halloysite, layered double hydroxide and smectites (Abdullayev and Lvov, 2010; Zhang et al., 2013; Tana et al., 2021). In the particular case of smectites, which are layered clay minerals, it is possible to take advantage of their swelling interlayer spaces to store various chemical species (Aranda et al., 2014; Ruiz-Hitzky and Casal, 1978). Moreover, several studies in the literature have already reported their use for the encapsulation of corrosion inhibitors (Abdullayev and Lvov, 2010; Zhang et al., 2013). Unfortunately, only cationic chemical species can be intercalated in significant amounts, since smectites are cation exchangers (Ngassa et al., 2014; Yanke et al., 2020). However, corrosion inhibitors (especially those used to protect copper) are mainly neutral compounds (Sherif, 2012; Qiang et al., 2017). Moreover, it is difficult to implement a strategy to avoid the fast release of the intercalated inhibitor once the composite material is introduced in the corrosive medium.

In this work, the intercalation of butylimidazole (Bim) (a compound recognized for its anticorrosive properties towards copper) in the interlayer space of a Cameroonian smectite is presented. The ability of the composite material to protect copper against corrosion in a Na_2SO_4 medium is subsequently studied, with emphasis on the controlled release of butylimidazole in the corrosive medium.

The strategy will consist in taking advantage of the basic properties of Bim to prepare butylimidazolium and therefore facilitating its intercalation in the interlayer space of the smectite by cationic exchange mechanism. In a concentrated Na_2SO_4 solution, the release of butylimidazole is expected to be favoured by the cationic exchange with sodium ions but also by the deprotonation of butylimidazolium, due to the acid-base equilibrium. Practically, once the composite material prepared and characterized by XRD, FTIR and TGA, its performance with respect to the protection of copper against corrosion will be evaluated by usual

electrochemical methods (Open-circuit chronopotentiometry, polarization curves, and electrochemical impedance spectroscopy).

2. Material and methods

2.1. Chemicals

Butylimidazole (Bim) (98%) was obtained from Sigma Aldrich and anhydrous sodium sulphate (99%) from Acros Organics. All other chemicals were of analytical grade. Aqueous solutions were prepared using deionised water (18.2 MΩ cm).

The Sabga clay mineral used in this study was collected in Sabga deposit (North-West region of Cameroon in Central Africa) and was well-described elsewhere (Tonle et al., 2003). The clay contains mainly smectites and present a cationic exchange capacity of 78 cmol kg^{-1} and specific surface area of 86 m^2 g^{-1}. The mineralogical composition showed mainly SiO_2 (63.4%), Al_2O_3 (15.6%), Fe_2O_3 (4.2%), MgO (0.2%), CaO (0.7%), Na_2O (0.4%), K_2O (2.3), TiO_2 (0.2%), (L.I. (13.8%) and trace amounts of P_2O_5 and MnO (Tonle et al., 2003). The copper rod (diameter of 4 mm) used as working electrode was of high purity, and adapted from a Tacussel copper based potentiometric electrode.

2.2. Clay mineral modification

The Na^+-saturated Sabga clay (Sg) with particle size < 2µm was obtained according to the procedure previously described in the literature (Yanke et al., 2017). Practically, 1 g of the fine fraction (< 2µm) collected by sedimentation was dispersed in 100 mL of sodium chloride 1 M and stirred at ambient temperature for 24 h. The solid was separated by centrifugation and free sodium ions removed by successive centrifuge washing using deionised water, followed by dialysis.

In a round bottom flask, 100 mL of Bim 0.2 M and 100 mL of HCl 0.2 M were mixed to obtain 200 mL of $BimH^+$ 0.1 M. 3 g of Sg was then dispersed in the solution and the mixture stirred for 3 days. The solid was then recovered by centrifugation (5000 rpm for 5 min) and washed several times by centrifugation using deionised water. The solid was oven-dried overnight at 80°C and the resulting material named Sg-Bim stored in a sealed vial for further use.

2.3. Characterization

XRD measurements were performed at room temperature on powder samples with a X'Pert Pro instrument from PANalytical (Malvern, United Kingdom) equipped with a PIXcel real-time multiple strip detector (active length=3.347° 2θ) over the 2° – 70° (2θ) range, using CuKα radiation (λ=1.542 Å). A step size of 0.013° (2θ) and a time per step of 218 s were applied for the measurements. The divergence slit, the anti-scatter slit, and the two Soller slits were 0.0625°, 0.125°, and 2.3°, respectively.

TGA analysis were performed on a Mettler – Toledo TGA/DSC1 LF1100 (Switzerland) in the temperature range 30°C to 1000°C at a heating rate of $10°C \cdot min^{-1}$ in air flow ($100 mL \cdot min^{-1}$).

Fourier Transform Infrared (FTIR) spectra (average of 40 consecutive scans) of the clay minerals were recorded on KBr pellets with a resolution of 4 cm^{-1} on a Bruker Alpha spectrometer in transmission mode.

2.4. Corrosion inhibition experiments

Electrochemical monitoring of copper corrosion was performed in two steps:

(i) Open circuit release of Bim in the sodium sulphate solution. During this step, a known amount of Sg-Bim was dispersed in 50 mL of a 0.1 M Na_2SO_4 solution and stirred for a set release time. Solid residue was then separated by centrifugation at 5000 rpm.

(ii) Electrochemical monitoring of copper electrode corrosion. The liquid obtained in the previous step, consisting of 0.1 M Na_2SO_4 and released Bim was then used for corrosion inhibition experiments.

For the electrochemical monitoring of copper electrode corrosion, three types of experiments were performed, using a saturated calomel electrode as reference, a high surface graphite rod as counter electrode and a copper rod (4 mm diameter) as working electrode. The surface of the working electrode was polished with 4000 grade SiC paper and rinsed with deionised water. The unexposed lateral surface was protected from electrolyte infiltration by a Teflon tape. The electrodes were connected to a PGSTAT 12 Autolab, from Eco Chemie, monitored by the GPES software for potentiometric or galvanostatic measurements. The FRA software was used for the EIS experiments.

- Corrosion potential was determined by open circuit chronopotentiometry. The open circuit potential of the copper electrode was continuously measured as a function of the immersion time.

- Polarisation curves were recorded after 1 h immersion of the electrode in corrosive solution to obtain a stable corrosion potential. Linear sweep voltammogram was then recorded at 1 mV s^{-1} in the potential range -0.4 V to 0.3 V. The corrosion efficiency (η_{Icor}) was obtained from this experiment by using corrosion current densities obtained with or without corrosion inhibitor (J_{cor}^{0} and J_{cor}^{Inh} respectively) using Equation 1 (Harrington and Devine, 2009) :

$$\eta_{Jcor} = \left(1 - \frac{J_{cor}^{inh}}{J_{cor}^{0}}\right) \times 100 \qquad \text{(Eq.1)}$$

- EIS experiments were performed in the frequency range 10 kHz to 10 mHz (with an applied amplitude of 10 mV).

3. Results and discussion

3.1. Encapsulation of butylimidazole in the interlayer space of Sabga clay (Sg)

The modification of the clay mineral by butylimidazole (Bim) was followed by XRD, TGA and FTIR spectroscopy.

XRD traces of the Na^+-exchanged Sabga clay mineral before and after modification by Bim are depicted in Figure 1.

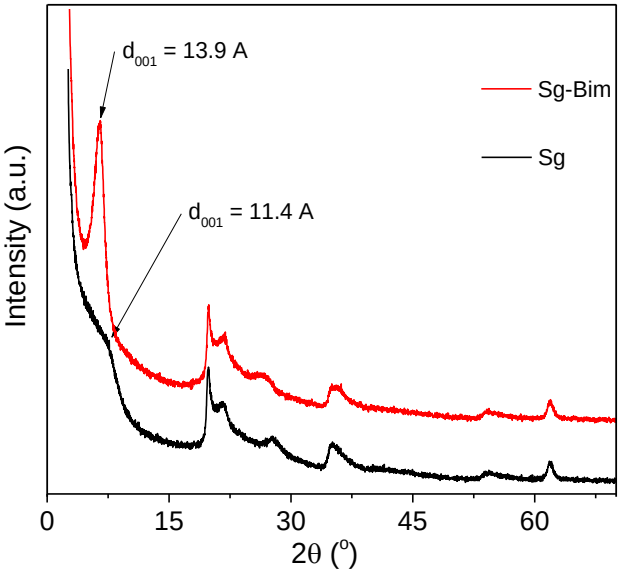

Figure 1. Powder XRD patterns of Sg and Sg-Bim.

The XRD traces of Sg displayed a d_{001}-value of 11.4 Å, characteristic of hydrated sodium ions present in the interlayer space (Ferrage et al., 2005). After reaction with Bim, the peak of the 001 diffraction plane became more intense and much better defined, which characterized a more regular stacking. This phenomenon was due to the organophilic property of Bim, less sensitive to atmospheric humidity changes. These functionalized surfaces subsequently serve as directing agents that promote layers aggregation. In addition, the d_{001} increases substantially (13.9 Å). This change in the average basal distance indicated the insertion of a compound in the interlayer

161 space. This increase of d_{001} of 2.5 Å would indicate that Bim preferentially adopts a planar
162 orientation between the layers of Sg.

163 FTIR spectra of Sg and Sg-Bim are presented in Figure 2 (A). The spectrum of Sg shows the
164 characteristic bands of smectites: stretching vibration band of structural O-H at 3632 cm^{-1},
165 vibration bands of Si-O at 1105 cm^{-1} and 1050 cm^{-1}. The broad and intense band at 3450 cm^{-1}
166 and that at 1640 cm^{-1} were assigned to the vibrations (stretching and bending respectively) of
167 water molecules adsorbed on the external surfaces or present in the interlayer space of the clay
168 mineral (Yanke et al., 2017; Yanke et al., 2020). In addition to these characteristic bands, Sg-
169 Bim presents three well-define bands at 2960 cm^{-1}, 2935 cm^{-1} and 2872 cm^{-1} due to the
170 stretching vibrations of C-Hs of the butyl group of Bim. The presence of the vibration band of
171 the C-H located on the imidazole ring at 3108 cm^{-1} was also observed. The vibration bands of
172 the aliphatic C-H present wave numbers equivalent to those obtained on pure Bim (Figure 2
173 (A)).

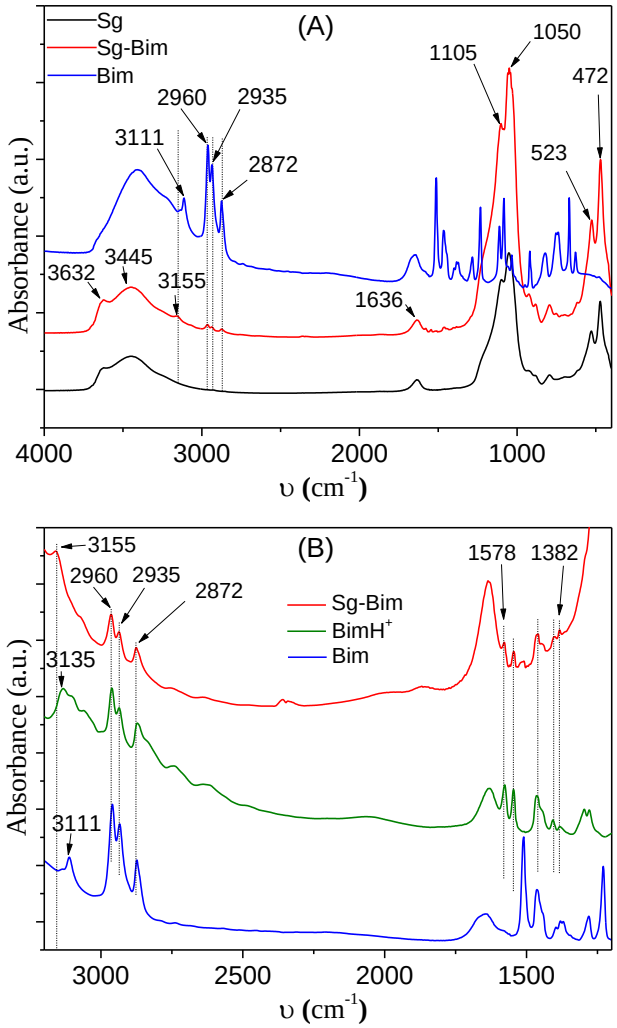

174

175 **Figure 2.** (A) FTIR spectra of Sg, Sg-Bim and Bim in the range 4000 cm^{-1} to 400 cm^{-1}. (B)

176 FTIR spectra of Sg-Bim, $BimH^+$ and Bim in the range 3200 cm^{-1} to 1200 cm^{-1}.

177

178 In the particular case of the C-Hs of the imidazole ring, a strong displacement of the band (up

179 to 44 cm^{-1}) was observed once adsorbed on the clay mineral (From 3111 cm^{-1} for Bim to 3155

180 cm^{-1} for Sg-Bim). Significant differences were also observed in the range 1600 cm^{-1} to 400 cm^{-1}

181 [1]. These differences can be explained by the strong interactions between these groups and the

182 functionalities of the clay mineral, leading to the modification of the vibration frequency of the

183 C-H bond of the imidazole ring. The protonation of Bim during the preparation of the material

184 could also explain the phenomenon. To verify the last hypothesis, the FTIR spectrum of ‘’pure’’

protonated Bim ($BimH^+$) using an equimolar amount of HCl was recorded (full spectrum presented in Figure S01). Figure 2 (B) shows the superposition of the spectra of Sg-Bim, Bim and $BimH^+$ in the range 3200 cm^{-1} to 1200 cm^{-1}. Surprisingly, regardless of the C-H vibration bands of the aliphatic carbons (between 2960 cm^{-1} and 2872 cm^{-1}), Bim and $BimH^+$ displayed completely different spectra. This is the proof that the protonation of the imidazole ring strongly modifies the vibration frequencies of the bonds directly involved in this cycle (named C=C, C=N and C-H).

On the spectrum of Sg-Bim in the range 1600 cm^{-1} to 1200 cm^{-1}, new vibration bands appear and were perfectly superimposed on those of $BimH^+$. This is the proof that Bim intercalates within Sg layers mainly in its protonated form ($BimH^+$). Moreover, the displacement of the vibration band associated to the imidazole ring C-H was observed on $BimH^+$ (from 3111 cm^{-1} to 3135 cm^{-1}). However, this displacement remains less important compared to that observed on Sg-Bim (3155 cm^{-1}). This suggests that the C-H vibration band of the imidazole ring is affected both by protonation and the interactions with the clay mineral functionalities.

The TGA traces (as well as the derived curves) of the clay mineral before and after modification are plotted in Figure 3. Sg displays three mass losses. The first centered at 62ºC (8.4%) corresponds to the loss of surface and intercalated water molecules. This significant mass loss reflects the strong hydrophilic character of Sg. This higher value compared to those usually reported in the literature is certainly due to the important humidity of the environment during the analyses. This result is in perfect agreement with the important d_{001}-value obtained during XRD characterization. The two successive mass losses with maximums at 444ºC and 620ºC are assigned to the dehydroxylation of the clay mineral. This two-step dehydroxylation is a characteristic of smectites which present both cis and trans-vacant configuration in the octahedral sheet (which is the case of Sg). It explains then the different amounts of energy needed to achieve dehydroxylation.

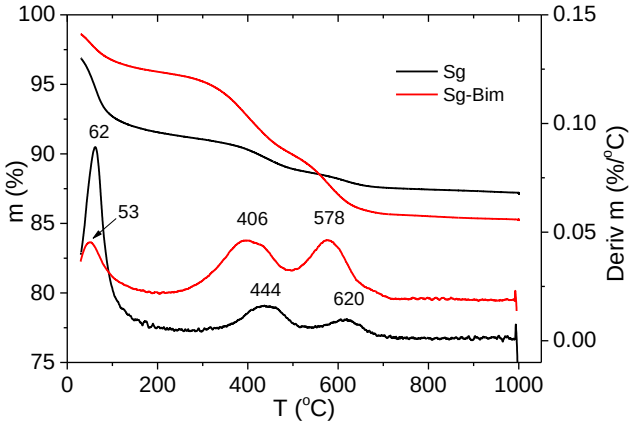

Figure 3. TGA traces and derivative curves recorded under air of Sg and Sg-Bim.

Sg-Bim also presents three mass losses. Dehydration occurs at 53°C (4.1%). This mass loss two times less important than that recorded on Sg, reflects a decrease of the hydrophilicity of the material after modification. Bim being a very water-soluble compound, this result could also be explained by considering the intercalation of $BimH^+$ in the interlayer space of Sg which leads to substitution of hydrated Na^+ ions. Therefore, intercalation would occur not only with a loss of the interlayer cations, but also a loss of most of the water molecules surrounding these cations.

Scheme 1 (A) illustrates the intercalation process of $BimH^+$. The two other mass loss events (406°C and 578°C) shifted to lower temperatures compared to pristine Sg sample. They could be attributed to the intercalation of Bim. The event with maximum at 406°C comprises the decomposition of Bim. One should note that Bim's mass loss occurs at a temperature largely above its boiling point (244.8°C). Such thermal stability is due to the strong interactions between this compound and the clay mineral. Such behaviour is frequent after the intercalation of organic compounds in the interlayer space of layered clay minerals (Ngnie and Dedzo, 2020; Dedzo et al., 2017).

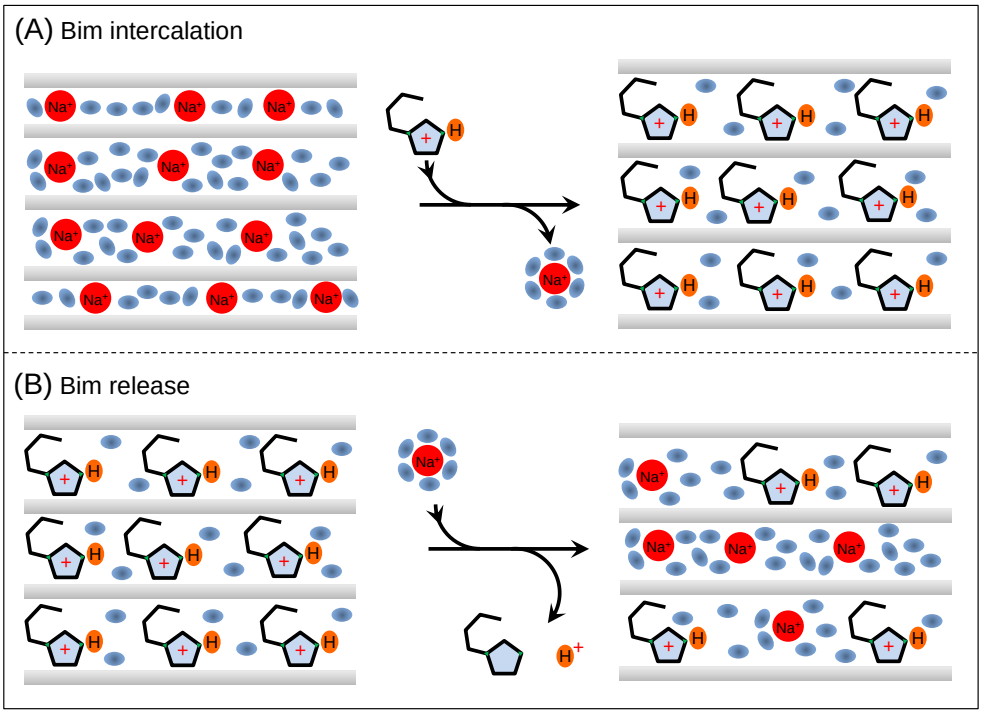

Scheme 1. (A) $BimH^+$ intercalation and (B) $BimH^+$ release following a guest-host displacement mechanism.

TGA analysis can be used for the accurate quantification of some organic modifiers. Since Bim can be completely degraded during carbonization, it is possible from the residual mass obtained at the end of the analysis (obtained after complete combustion at 1000°C) to determine the amount of modifier initially present in the sample based on Equation 2.

$$m = \frac{m_{200} \cdot m_{Sg(1000)}}{m_{Sg(200)}} - m_{(1000)} \qquad \text{(Eq.2)}$$

Where m (%) represents the mass percentage of Bim, m_{200} (%) and $m_{Sg(200)}$ (%) the mass percentages of Sg-Bim and Sg respectively after the loss of physisorbed water (at 200°C), $m_{(1000)}$ and $m_{Sg(1000)}$ the mass percentages of Sg-Bim and Sg respectively at the end of thermogravimetric analysis (complete carbonisation/dehydroxilation at 1000°C). As a result, Sg-Bim contains 6.1% of Bim, corresponding to 0.48 mmol/g of initial hybrid material.

3.2. Application for copper corrosion inhibition in concentrated aqueous sodium sulphate solution

The effect of Bim against copper corrosion in a corrosive saline environment is well recognized (Durainatarajan et al., 2018). Preliminary experiments using Bim as copper corrosion inhibitor in a 0.1 M sodium sulphate solution confirmed this efficiency (Figure S01 shows the variation of the inhibition percentage of the copper electrode as a function of Bim concentration in a 0.1 M Na_2SO_4 solution).

In this work, Bim molecules intercalated in the interlayer space of the Sabga clay were released in a corrosive environment in order to protect a copper rod against corrosion. The corrosion process was followed by electrochemistry. The experimental parameters such as release time, amount of inhibitor and temperature were varied in order to study the corrosion inhibition process.

3.2.1. Effect of the release time of Bim on copper corrosion inhibition

3.2.1.1. Corrosion potential.

The real time measurement of the corrosion potential of copper electrode as a function of immersion time was performed for different Bim release times from Sg-Bim (Figure 4 (A)).

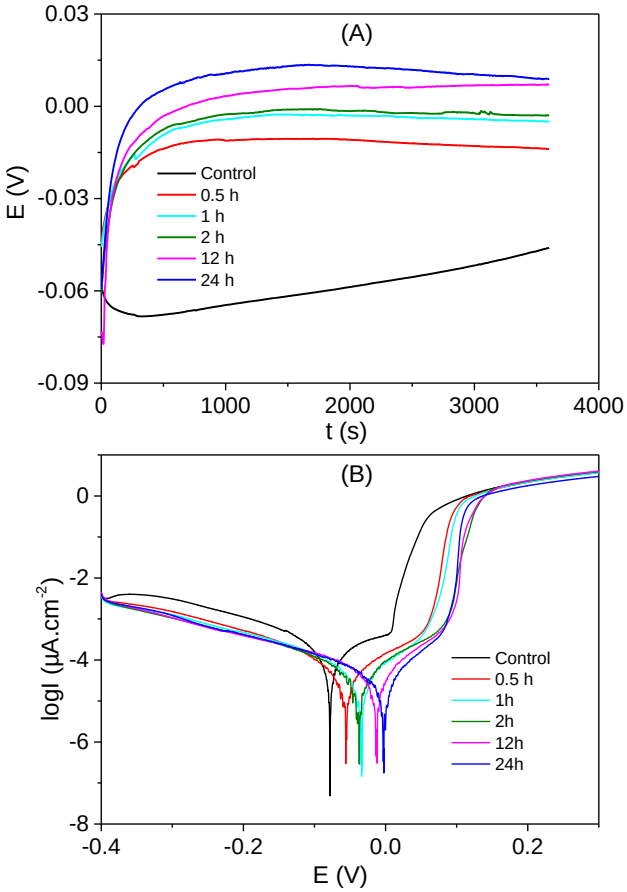

Figure 4. (A) Variation of the corrosion potential of copper electrode as a function of immersion time for different Bim release times from Sg-Bim. (B) Polarization curves plotted after 1 hour of immersion in the electrolytic solution, at a scanning rate of 1 $mV.s^{-1}$ for different Bim release times from Sg-Bim. The release and electrochemical measurements were performed in a 0.1 M Na_2SO_4 solution.

The fast decrease of the corrosion potential in the absence of Sg-Bim, just after the immersion of the copper electrode, was assigned to the dissolution of the copper oxide layer initially present. The dissolution was the consequence of the action of the sulphate anions present in the corrosive medium (Hamed, 2010). The trends of curves obtained when using Sg-Bim showed different tendencies. During the first 15 min, the potential increase indicated the gradual stabilization of the oxide layer initially present. This was followed by an almost stationary state

due to the achievement of a constant corrosion rate. The potential at these stationary states represent the corrosion potentials. In the absence of Sg-Bim, after 1 hour of immersion in sodium sulphate solution, the open circuit corrosion potential reported was -46 mV. In the presence of Sg-Bim, this potential increased with the release time to reach a maximum value of 9 mV after 24 h. This increase reflected the metal protection against corrosion, due to the presence of Bim released in solution by the hybrid material Sg-Bim. This first result suggested that Bim is effectively released from Sg-Bim when dispersed in the sodium sulfate solution. Furthermore, the amount of Bim in solution increased with the release time.

To confirm this hypothesis, FTIR of the material after 24 h release was recorded (Figure S02). It was found that the absorption bands of $BimH^+$ were still present but were by far less intense. This proved that after 24 h, large amounts of Bim were released in solution. Surprisingly, the XRD traces (Figure S03) of Sg-Bim after 24h of release (Sg-Bim/24h) presented a d_{001}-value closed to that of Sg-Bim (13.9 Å). This suggested that there was a partial removal of intercalated Bim, but not important enough to promote the collapse of adjacent layers. Scheme 1 (B) represents the exchange process during the release and the probable arrangement of $BimH^+$ in the interlayer space before and after the release.

3.2.1.2. Polarisation curves.

More accurate and quantitative corrosion parameters were obtained from polarization curves (plotted after 1 hour of immersion in a 0.1 M Na_2SO_4 solution, at a scanning rate of 1 mV s^{-1}) recorded for release times ranging between 0.5 h and 24 h.

All the curves displayed the same trend and were subdivided into four distinct sections (Pourbaix 1974; Scendo, 2008) :

(i) The cathodic branch characterized by oxygen reduction at the electrode surface according to equation 3;

$$O_2 + 2H_2O + 4e^- \leftrightarrow 4HO^- \quad \text{(Eq.3)}$$

(ii) The first plateau of the anodic branch assigned to copper oxidation to yield Cu(I) according to equation 4.

$$Cu \leftrightarrow Cu^+ + e^- \quad \text{(Eq.4)}$$

The reaction of Cu^+ with HO^-, followed by dehydration yielded Cu_2O. Thus, Equation 3 and 4 can be summarized as the formation of Cu_2O following copper oxidation by dissolved oxygen according to equation 5;

$$4Cu + O_2 \rightarrow 2Cu_2O \quad \text{(Eq.5)}$$

(iii) The fast oxidation that follows the formation of the first plateau was associated to the oxidation of Cu_2O to CuO by dissolved oxygen according to the general equation 6.

$$2Cu_2O + O_2 \rightarrow 4CuO \quad \text{(Eq.6)}$$

(iv) The second plateau formed thereafter is a diffusion plateau limited by the constant formation of CuO.

In the presence of Sg-Bim, both cathodic and anodic currents were less important compared to the signal recorded without the inhibitor. Sg-Bim can thus be considered as a mixed inhibitor (cathodic and mostly anodic inhibitor) (Hamed, 2010; Xu et al., 2018), due to its ability to promote the formation of a strong protective film capable to reduce the rate of copper oxidation and prevent the access of oxygen to the metal surface. One can assume that the presence of Bim in solution stabilizes the Cu_2O film, which is much more effective than CuO for protecting the metal against corrosion. The positive effect of Bim on protection was further confirmed by the

overvoltage required to oxidize Cu_2O to CuO in the presence of inhibitor. Of course, these phenomena become much more important for higher release times (increasingly important amounts of Bim in solution).

For a quantitative analysis of these potentiodynamic curves, a series of parameters (corrosion current densities (j_{cor}), anodic and cathodic Tafel slopes (b_a and b_c) and polarization resistances (R_p)) were extracted and summarized in Table 1.

Table 1. Electrochemical parameters obtained from polarization curves plotted during the study of the effect of Bim release time.

	J_{cor} ($\mu A.cm^{-2}$)	[Bim] ($mg.L^{-1}$)	b_a (mV/dec)	b_c (mV/dec)	R_p ($\times 10^5 \Omega.cm^2$)	η_{Jcorr} (%)
Control	0.140	- - -	160.3	111.0	1.42	----
0.5h	0.039	6.19	100.9	104.9	4.20	72.14
1h	0.034	8.04	86.0	103.3	4.34	75.71
2h	0.032	9.02	71.0	113.0	4.70	77.14
12h	0.028	11.62	75.3	130.2	5.35	80.00
24h	0.027	12.45	87.2	109.1	5.45	80.70

After 30 min of release, the corrosion current was 3.5 times less important (corresponding to an inhibition percentage of 72.1%). This is a proof that Bim is effectively released in solution and protects copper against corrosion. The corrosion current density thus gradually decreases with the release time, but with slower rate. After 24 hours, the inhibition percentage was 80.7%. On the other hand, as expected, the polarization resistance increases (from 1.42×10^5 Ω cm^2 to 5.45×10^5 Ω cm^2) with the release time.

Using the corrosion current variation curve obtained when the effect of controlled amounts of Bim was evaluated during corrosion experiments as a standard curve (Equation as inset of Figure S01), the amounts of Bim released by Sg-Bim as a function of time were determined

and presented in Table 1. After only 30 min, the amount of Bim released was equivalent to 6.19 mg L^{-1}. After 24 h, the amount released increases by a factor of 2 (12.45 mg L^{-1}). This result is another direct proof of the release of Bim from Sg-Bim, as a function of time.

3.2.1.3. Electrochemical impedance spectroscopy.

Figure 5 (A) depicts the Nyquist diagrams, recorded after 1 hour of immersion in the absence and in the presence of Bim in 0.1 M Na_2SO_4 medium for various release times. The diagrams showed capacitive loops at high frequency and a Warburg impedance at low frequencies (case of the control experiment without Sg-Bim). The loop at high frequency can be attributed to the charge transfer at the metal surface. The diameter of the high frequency loop increases with the amount of Sg-Bim used and the release time applied. This indicates that the protection of the metal against corrosion increases with the release time as indicated by the analysis of the polarization curves. Without inhibitor, the Bode diagram (Figure 5 (B)) shows the presence of two time constants (the first around 1000 Hz and the second around 0.1 Hz). In the presence of Bim, only the time constant at high frequency (around 1000 Hz) was observed and assigned to a charge transfer.

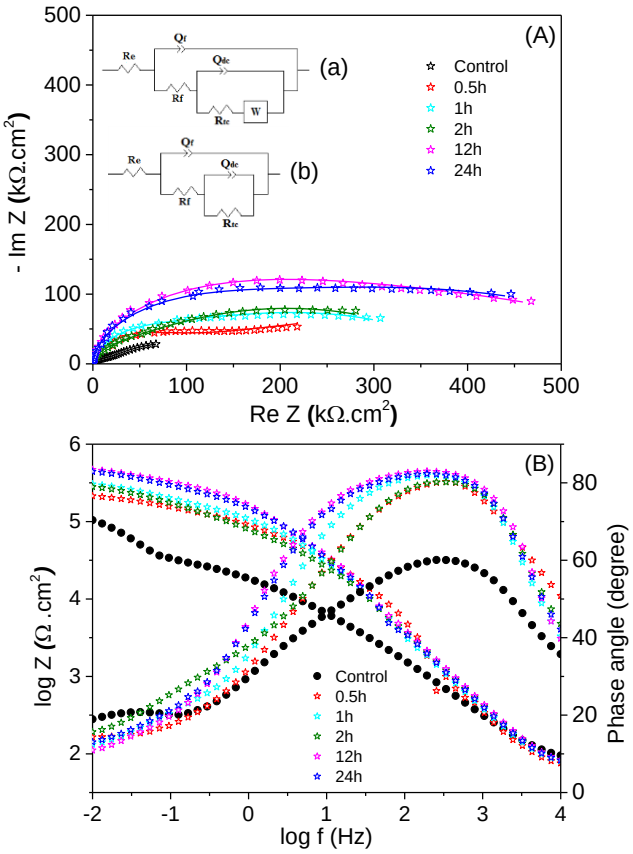

Figure 5. (A) Nyquist and (B) Bode diagrams plotted in the frequence range 10 kHz to 10 mHz for different Bim release times from Sg-Bim. The release and electrochemical measurements were performed in a 0.1 M Na_2SO_4 solution. The equivalent electrical circuits used for data fitting (plain lines of (A)) in Control (a) and Sg-Bim release (b) experiments are presented as Inset in (A).

The non-appearance of the second time constant at low frequency was explained by the poor diffusion of corrosive species through the less porous protective layer (probably a mixture of Cu_2O and Bim) (Zarrouk et al., 2013; Bozorg et al., 2014; Hachelef et al., 2017).

For a more precise interpretation of the observed phenomena without inhibitor, the EIS data were simulated by considering an electrical circuit (circuit (a) of figure 5 (A)) describing a charge transfer coupled to a diffusion process (Van Ingelgem et al., 2007). In the presence of

Bim, the diffusion process was minimized by removing the Warburg component in the equivalent electrical circuit (circuit (b) of Figure 5 (A)). The constant obtained from simulation (Fitting curves of Figure 5 (A)) using these two electrical circuits are presented in Table 2.

Table 2. Electrochemical parameters obtained from EIS data during the study of the effect of Bim release time.

	R_{ct} ($k\Omega$)	$Q_f \times 10^{-6}$ ($S^{\alpha f}\ \Omega^{-1}\ cm^{-2}$)	$Q_{dl} \times 10^{-6}$ ($S^{\alpha dl}\ \Omega^{-1}\ cm^{-2}$)	α_{dl}	C_{dl} ($\mu F\ cm^{-2}$)	$\chi^2 \times 10^{-3}$	η_{Rct} (%)
Control	58.78±0.03	8.454±0.006	83.67±0.02	0.58±0.06	265±63	3.1	----
0.5 h	278.4±0.5	0.732±0.001	9.572±0.005	0.64±0.03	16.6±0.9	2.8	78.9±0.4
1 h	312.9±0.2	0.5817±0.0004	6.154±0.004	0.73±0.06	7.8±0.6	6.9	81.2±0.2
2 h	356.10±0.09	0.513±0.001	5.863±0.002	0.77±0.04	7.3±0.4	3.9	83.49±0.04
12 h	406.5±0.1	0.4721±0.0003	5.813±0.003	0.82±0.05	7.0±0.4	5.2	85.54±0.04
24 h	452.6±0.1	0.5208±0.0002	4.831±0.002	0.81±0.05	5.8±0.3	4.7	87.01±0.04

These data were used to calculate both the inhibitory efficiency η_{Rct} and the double layer capacity C_{dl} ($F.cm^{-2}$) from equations 7 and 8 (Harrington and Devine, 2009):

$$\eta_{Rct} = (1 - \frac{R_{ct}^{0}}{R_{ct}^{inh}})\ 100 \qquad \text{(Eq.7)}$$

$$C_{dl} = (Q_{dl}\ R_{ct}^{1-\alpha_{dl}})^{1/\alpha_{dl}} \qquad \text{(Eq.8)}$$

R_{ct}^{0} and R_{ct}^{inh} (ohm) represent respectively the charge transfer resistance obtained without inhibitor and in the presence of inhibitor, Q_{dl} ($S^{\alpha dl}\ \Omega^{-1}\ cm^{-2}$) and α_{dl} are respectively the constant phase elements and the homogeneity parameter associated to the double layer.

The increase of R_{ct} and decrease of C_{dl} (indicating the increase of the efficiency of the protective layer) in the presence of increasing amounts of Bim, indicate an improvement of the effectiveness of the protection against corrosion.

The values of the inhibitory efficiency obtained from the charge transfer resistances are greater (maximum of 87.0%) compared to that determined from the corrosion currents (Maximum of 80.7%). However, the overall trend is similar: significant increase of the inhibitory efficiency as a function of release time for a given amount of Sg-Bim dispersed in solution.

3.2.2. Effect of the amount of Sg-Bim in copper corrosion

The effect of the amount of Sg-Bim used for Cu inhibition in 0.1 M Na_2SO_4 solution was investigated. The release time was kept constant at 24 hours. Figure 6 shows the polarization curves obtained for Sg-Bim concentrations ranging between 50 mg L^{-1} and 500 mg L^{-1} as well as the variation of corrosion current densities against the concentration of the organoclay used. Electrochemical parameters obtained from these curves are summarized in Table S01.

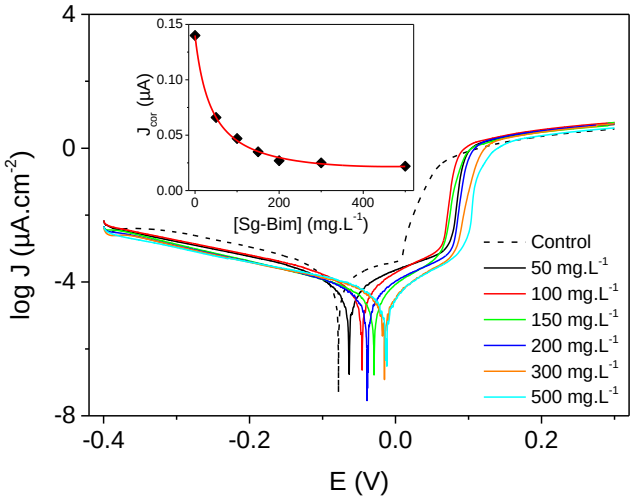

Figure 6. Polarization curves plotted after 1 hour of immersion in the electrolytic solution, at a scanning rate of 1 $mV.s^{-1}$ for different Sg-Bim concentrations. The release and electrochemical measurements were performed in a 0.1 M Na_2SO_4 solution and the release time set at 24 h. Inset, variation of corrosion current density against Sg-Bim concentration.

393 Generally, the curves recorded in the presence of inhibitor displayed similar trend and showed
394 anodic and cathodic currents below those of the curve recorded without inhibitor. Furthermore,
395 the corrosion currents decrease sharply with the amount of Sg-Bim used. Above 200 mg L^{-1},
396 this decrease becomes less important. This indicates an optimal protection of the metal above
397 this concentration for the experimental conditions used. The corrosion current density decreases
398 as the inhibitor concentration increases. This indicates an overall improvement of the protection
399 of the metal against corrosion.

400 These results confirm once again that Sg-Bim effectively releases the inhibitor in the corrosive
401 solution and that this compound is effective in protecting copper against corrosion in
402 concentrated sulphate medium. On the other hand, for equivalent times, a large mass of Sg-Bim
403 releases more corrosion inhibitor. This is proof that the clay mineral Sg-Bim serves as a
404 reservoir for the encapsulation of Bim.

405 **3.2.3. Effect of temperature on the efficiency of Sg-Bim in copper corrosion**

406 The effect of temperature on the corrosion process was evaluated in order to determine
407 thermodynamic parameters allowing the elucidation of the nature of interactions between Bim
408 and the protective layer (Figure 7). Electrochemical parameters obtained from these curves are
409 summarized in Table S02. Sg-Bim concentration of 200 mg L^{-1} and a release time of 24 h were
410 set for this study.

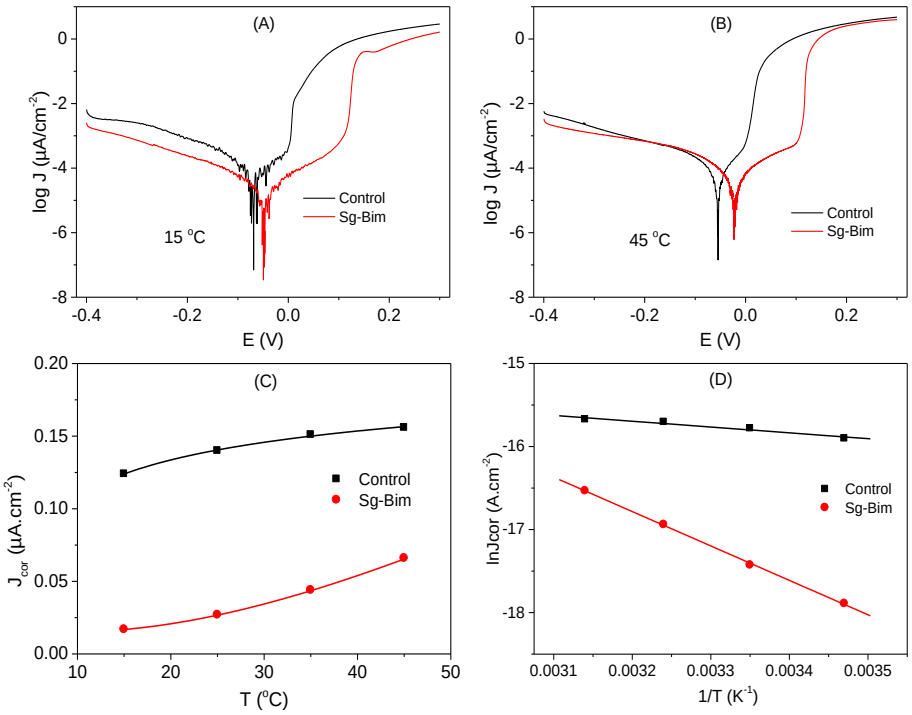

411

412 **Figure 7**. Comparison of the polarization curves recorded after 1 hour of immersion in the
413 electrolytic solution at a scanning rate of 1 mV.s^{-1} without or with Sg-Bim (200 mg.L^{-1}) at 15
414 °C (A) and 45 °C (B). The release and electrochemical measurements were performed in a 0.1
415 M Na_2SO_4 solution and the release time set at 24 h. (C) Variation of the corrosion current
416 density against temperature. (D) Arhenius plots without or with Sg-Bim (200 mg.L^{-1}).

417

418 Both in the absence and in the presence of Sg-Bim, the corrosion current densities increase with
419 temperature. In the absence of inhibitor, thermal agitation following temperature increase tends
420 to weaken the protective film on the surface of the metal and at the same time prevents its
421 formation at a sufficient rate to protect the copper rod against corrosion.

422 In the presence of inhibitor, the thermal agitation also renders difficult the adsorption of Bim
423 onto copper oxides present on the metal surface. This reflects the physical nature of the
424 adsorption (physisorption) of Bim on the surface of copper oxides (Hamed, 2010). Indeed,
425 physisorption is a consequence of Van der Waals-type interactions between the surface of the

metal oxide layer and the Bim molecules (Landolt, 2007). These interactions are very sensitive to thermal agitation and break down as soon as it increases.

The corrosion current can be expressed as a function of the activation energy using an equation similar to that of Arrhenius (Hamed, 2010; Ngouné, 2019) (Equation 9).

$$J_{cor} = A \exp\left(-\frac{E_a}{RT}\right) \quad \text{(Eq.9)}$$

Where A represents the Arrhenius constant, E_a (J mol^{-1}) the activation energy, R (8.314 J mol^{-1} K^{-1}) the ideal gas constant and T (K) the temperature.

The value of E_a in the presence of inhibitor (34.44 kJ mol^{-1}) was approximately six times greater than that obtained in the absence of inhibitor (5.82 kJ mol^{-1}). This result confirms once again that physisorption is the mechanism of adsorption of Bim at the surface of copper in this study (Scendo, 2005).

4. Conclusion

Butylimidazole (Bim) was successfully intercalated in the interlayer space of a Cameroonian smectite clay mineral by the guest displacement of exchangeable hydrated sodium ions. The material (Sg-Bim) was successfully applied as a copper corrosion inhibitor in concentrated sodium sulfate medium (0.1 M). Once dispersed in the corrosive medium, butylimidazolium was gradually replaced by the cations of the saline solution (Na^+ in the present case). This exchange was favoured by the large concentration gradient of sodium and butylimidazolium, existing between the solid (Sg-Bim) and the liquid phase (Na_2SO_4 solution). Thus, it was the Bim released in solution that protected the copper against corrosion from sulfate ions. This work offers many possibilities for the use of smectites as nanocontainers for the encapsulation of neutral corrosion inhibitors.

Acknowledgements

AUF (Agence Universitaire de la Francophonie) is acknowledged for the grant AUF DRACGL-2017-006 offered to C.P. Nanseu-Njiki. The authors also acknowledge the International Science Program (ISP) – Sweden through funding provided to the African Network of Electroanalytical Chemists (ANEC). XRD and TG experiments were performed on the technical platforms of IS2M. The authors are grateful to Laure Michelin and Habiba Nouali for their contributions.

References

Abdullayev, E., Lvov, Y., 2010. Clay nanotubes for corrosion inhibitor encapsulation: release control with end stoppers. J. Mater. Chem. 20, 6681-6687.

Aghzzaf, A.A., Rhouta, B., Steinmetz, J., Rocca, E., Aranda, L., Khalil, A., Yvon, J., Daoudi, L., 2012. Corrosion inhibitors based on chitosan-heptanoate modified beidellite. Appl. Clay Sci. 65, 173-178.

Aranda, P., Casal, B., Fripiat, J.J., Ruiz-Hitzky, E., 1994. Intercalation of Macrocyclic Compounds (Crown Ethers and Cryptands) into 2:1 Phyllosilicates. Stability and Calorimetric Study. Langmuir 10, 1207-1212.

Bidi, M.A., Azadi, M., Rassouli, M., 2021. An enhancement on corrosion resistance of low carbon steel by a novel bio-inhibitor (leech extract) in the H_2SO_4 solution. Surf. Interfaces 24, 101159.

Bozorg, M., Farahani, T.S., Neshati, J., Chaghazardi, Z., Mohammadi, Z.G., 2014. Myrtus communis as green inhibitor of copper corrosion in sulfuric acid. Ind. Eng. Chem. Res. 53, 4295-4303.

Damej, M., Kaya, S., Ibrahimi, B.E., Lee, H., Molhi, A., Serdaroğlu, G., Benmessaoud, M., Ali, I., Hajjaji, S.E., Lgaz, H., 2021. The corrosion inhibition and adsorption behavior of mercaptobenzimidazole and bis-mercaptobenzimidazole on carbon steel in 1.0 M HCl: Experimental and computational insights. Surf. Interfaces 24, 101095.

Dedzo, G.K., Nguelo, B.B., Tonle, I.K., Ngameni, E., Detellier, C., 2017. Molecular control of the functional and spatial interlayer environment of kaolinite by the grafting of selected pyridinium ionic liquids. Appl. Clay Sci. 143, 445-451.

Durainatarajan, P., Prabakaran, M., Ramesh, S., Periasamy, V., 2018. Surface protection of copper in 3% NaCl solution by using 1-(n-butyl) imidazole self-assembled monolayer. Mater. Today : Proc. 5, 16226-16236.

Ferrage, E., Lanson, B., Sakharov B., Drits, V., 2005. Investigation of smectite hydration properties by modeling experimental X-ray diffraction patterns: Part I. Montmorillonite hydration properties. Am. Mineral. 90, 1358-1374.

Gece, G., 2008. The use of quantum chemical methods in corrosion inhibitor studies. Corros. Sci. 50, 2981-2992.

Hachelef, H., Benmoussat, A., Khelifa, A., Meziane, M., 2017. Study of the propolis extract as a corrosion inhibitor of copper alloy in ethylene glycol/water 0.1 M NaCl. J. Fundam. Appl. Sci. 9, 650-668.

Hamed, E., 2010. Studies of the corrosion inhibition of copper in Na2SO4 solution using polarization and electrochemical impedance spectroscopy. Mater. Chem. Phys. 121, 70-76.

491 Harrington, S.P., Devine, T.M., 2009. Relation between the semiconducting properties of a
492 passive film and reduction reaction rates. J. Electrochem. Soc. 156, C154.

493 Landolt, D., 2007. Corrosion and surface chemistry of metals, first ed, CRC press, Lausanne.

494 Ngassa, G.B., Tonlé, I.K., Walcarius, A., Ngameni, E., 2014. One-step co-intercalation of
495 cetyltrimethylammonium and thiourea in smectite and application of the organoclay to the
496 sensitive electrochemical detection of Pb (II). Appl. Clay Sci. 99, 297-305.

497 Ngnie, G., Dedzo, G.K., 2020. A template approach for the multifunctionalization of the
498 interlayer space of kaolinite, Appl. Clay Sci. 198, 105858.

499 Ngouné, B., Pengou, M., Nouteza, A.M., Nanseu-Njiki, C.P., Ngameni, E., 2019.
500 Performances of alkaloid extract from Rauvolfia macrophylla Stapf toward corrosion
501 inhibition of C38 steel in acidic media. ACS Omega 4, 9081-9091.

502 Pourbaix, M., 1974. Atlas of electrochemical equilibria in aqueous solution, second ed.
503 NACE, Texas.

504 Qiang, Y., Zhang, S., Yan, S., Zou, X., Chen, S., 2017. Three indazole derivatives as
505 corrosion inhibitors of copper in a neutral chloride solution. Corros. Sci. 126, 295-304.

506 Ruiz-Hitzky, E., Casal, B., 1978. Crown ether intercalations with phyllosilicates. Nature 276,
507 596-597.

508 Scendo, M., 2005. Corrosion inhibition of copper by potassium ethyl xanthate in acidic
509 chloride solutions. Corro. Sci. 47, 2778-2791.

510 Scendo, M., 2008. Inhibition of copper corrosion in sodium nitrate solutions with nontoxic
511 inhibitors. Corros. Sci. 50, 1584-1592.

512 Sherif, E., 2012. Electrochemical and gravimetric study on the corrosion and corrosion
513 inhibition of pure copper in sodium chloride solutions by two azole derivative. Int. J.
514 Electrochem. Sci. 7. 1482-1495.

515 Tana, J.K.E. Balana, P., Birbilis, N., 2021. Advances in LDH coatings on Mg alloys for
516 biomedical applications: A corrosion perspective. Appl. Clay Sci. 202, 105948.

517 Tchio, O.R.W., Pengou, M., Baumier, C., Franger, S., Teillout, A.L., Mbomekallé, I.M., De
518 Oliveira, P., Nanseu-Njiki, C.P., Ngameni, E., 2020. Comparison between lacunary and
519 saturated keggin polyoxometalates as steel corrosion inhibitors in chloride solution:
520 contribution of the lacuna in the inhibition mechanism. ChemistrySelect 5, 10135-10143.

521 Tonle, I.K., Ngameni, E., Njopwouo, D., Carteret, C., Walcarius, A., 2003. Functionalization
522 of natural smectite-type clays by grafting with organosilanes: physico-chemical
523 characterization and application to mercury (II) uptake. Phys. Chem. Chem. Phys. 5, 4951-
524 4961.

525 Truc, T.A., Hang, T.T.X., Oanh, V.K., Dantras, E., Lacabanne, C., Oquab, D., Pébère, N.,
526 2008. Incorporation of an indole-3 butyric acid modified clay in epoxy resin for corrosion
527 protection of carbon steel. Surf. Coat. Technol. 202, 4945-4951.

528 Van Ingelgem, Y., Hubin, A., Vereecken, J., 2007. Investigation of the first stages of the
529 localized corrosion of pure copper combining EIS, FE-SEM and FE-AES. Electrochim. Acta
530 52, 7642-7650.

531 Verma, C., Quraishi, M., Ebenso, E., 2020. Quinoline and its derivatives as corrosion
532 inhibitors: A review. Surf. Interfaces 21, 100634.

533 Wang, Y., Zhang, D., 2011. Synthesis, characterization, and controlled release anticorrosion
534 behavior of benzoate intercalated Zn–Al layered double hydroxides. Mater. Res. Bull. 46,
535 1963-1968.

536 Winkler, D., Breedon, M., White, P., Hughes, A., Sapper, E., Cole, S., 2016. Using high
537 throughput experimental data and in silico models to discover alternatives to toxic chromate
538 corrosion inhibitors. Corros. Sci. 106, 229-235.

539 Xu, Y., Zhang, S., Li, W., Guo, L., Xu, S., Feng, L., Madkour, L., 2018. Experimental and
540 theoretical investigations of some pyrazolo-pyrimidine derivatives as corrosion inhibitors on
541 copper in sulfuric acid solution. Appl. Surf. Sci. 459, 612-620.

542 Yanke, J.G.M., Dedzo, G.K., Ngameni, E., 2017. Solvent effect on the grafting of an
543 organophilic silane onto smectite-type clay: Application as electrode modifiers for pesticide
544 detection, Electroanalysis 29, 1894-1902.

545 Yanke, J.G.M., Dedzo, G.K., Ngameni, E., 2020. Grafting of organophilic silane in the
546 interlayer space of acid-treated smectite: Application to the direct electrochemical detection of
547 glyphosate. Appl. Clay Sci. 188, 105513.

548 Yuan, M., Lu, J., Kong, G., 2010. Effect of SiO2: Na2O molar ratio of sodium silicate on the
549 corrosion resistance of silicate conversion coatings. Surf. Coat. Technol. 204, 1229-1235.

550 Zarrouk, A., Hammouti, B., Dafali, A., Bentiss, F.J.I., 2013. Inhibitive properties and
551 adsorption of purpald as a corrosion inhibitor for copper in nitric acid medium. Ind. Eng.
552 Chem. Res. 52, 2560-2568.

553 Zhang, Y., Shao, Y., Zhang, T., Meng, G., Wang, F., 2013. High corrosion protection of a
554 polyaniline/organophilic montmorillonite coating for magnesium alloys. Prog. Org. Coat. 76,
555 804-811.